

Tuning the Photonic Spin Hall Effect through vacuum-induced transparency in an atomic cavity

Muqaddar Abbas ^a, Yunlong Wang ^{a,*}, Feiran Wang ^b, Hamid R. Hamed ^c, Pei Zhang ^a

^a Ministry of Education Key Laboratory for Nonequilibrium Synthesis and Modulation of Condensed Matter, Shaanxi Province Key Laboratory of Quantum Information and Quantum Optoelectronic Devices, School of Physics, Xi'an Jiaotong University, Xi'an 710049, China

^b School of Science of Xi'an Polytechnic University, Xi'an 710048, China

^c Institute of Theoretical Physics and Astronomy, Vilnius University, Sauletekio 3, Vilnius 10257, Lithuania

ARTICLE INFO

Keywords:

Vacuum induced transparency
Atom cavity interaction
Cavity quantum electrodynamics
Photonic Spin Hall Effect

ABSTRACT

We present a method for manipulating the Photonic Spin Hall Effect (PSHE) by examining the characteristics of an atomic ensemble with two levels connected to a high-quality cavity. Although the cavity is initially in a vacuum state with no external excitation, a substantial change can be made to the atomic ensemble's probe response. A coherent effect analogous to electromagnetically induced transparency (EIT) arises when the cavity decay rate is significantly lower than the atomic dissipation rate and the collective atom-cavity interaction is robust. This results in reduced absorption of the two-level atoms in the cavity, even in the absence of external stimulation, a phenomenon known as vacuum-induced transparency, which in turn amplifies the PSHE. Furthermore, we explore how varying the atomic number density enhances the PSHE without altering the cavity's structure. These findings offer new prospects for applications in quantum electrodynamics within cavity systems.

1. Introduction

The Photonic Spin Hall Effect (PSHE) has become a cornerstone of spin photonics, facilitating the transverse spatial separation of light beams with opposite spin states through spin-orbit coupling [1,2]. Analogous to the electronic spin Hall effect, where spin-polarized electrons respond to an electric potential gradient, the PSHE replaces electrons with spin-polarized photons and a refractive index gradient as the driving force [3,4]. First theorized by Onoda et al. in 2004 [1], the PSHE gained further theoretical depth with the contributions of Bliokh and Bliokh [2]. Its experimental confirmation came in 2008 when Hosten and Kwiat employed weak measurement techniques to observe this phenomenon in optical systems.

The PSHE is now widely attributed to the spin-orbit coupling of photons, governed by the principle of angular momentum conservation in light [5,6]. In this effect, left- and right-circularly polarized photons experience distinct transverse shifts at the interface of a coherent medium due to spin-orbit interactions [7]. These shifts are influenced by the optical angular momentum and two distinct geometric phases [8]. The first is the spin-redirecting phase, or Rytov-Vlasimirskii-Berry phase, associated with changes in the wave vector's propagation direction. The second is the Pancharatnam-Berry phase,

which involves controlling photon polarization states to induce shifts in photon trajectories [8,9]. This technique is known for its robustness and ability to generate phase shifts that depend on the polarization orientation, making it valuable in spin-orbit coupled systems. The advantage of geometric phase manipulation is its relatively straightforward implementation and strong resilience to environmental disturbances.

However, the key limitation of geometric phase methods is that they often lack the ability to dynamically tune the PSHE across a wide range of conditions. While static geometric phase shifts can be controlled by varying polarization, achieving dynamic control over the spin-orbit coupling and spin-dependent displacement is more challenging.

A variety of mathematical and experimental methods have been developed to enhance the PSHE, including weak value amplification (WVA), which significantly magnifies the transverse spin-dependent displacement associated with the effect [10,11]. WVA has been widely explored to enhance the transverse spin-dependent displacement associated with the PSHE. In this approach, small shifts in photon trajectories are amplified through weak measurement, which can significantly magnify the effect [10,11]. This makes WVA highly sensitive to small variations in the spin-orbit interaction. However, WVA typically requires precise experimental control to avoid errors in measurement,

* Corresponding authors.

E-mail addresses: yunlong.wang@mail.xjtu.edu.cn (Y. Wang), feiran0325@xjtu.edu.cn (F. Wang), hamid.hamed@tfai.vu.lt (H.R. Hamed), zhangpei@mail.ustc.edu.cn (P. Zhang).

<https://doi.org/10.1016/j.chaos.2025.116292>

Received 8 January 2025; Received in revised form 23 February 2025; Accepted 9 March 2025

0960-0779/© 2025 Elsevier Ltd. All rights are reserved, including those for text and data mining, AI training, and similar technologies.

and its applicability may be limited by the strength of the weak values in certain setups. Furthermore, WVA often operates in the regime of small, linear displacements, and may not provide the same level of flexibility in dynamic tuning as other methods. Recently, interest has grown in leveraging the PSHE to control spin-dependent photon behavior across various optical media, driven by its potential for spin-level light manipulation in a wide range of applications [10,12–16]. Recently, researchers have examined in- and out-of-plane shifts in the PSHE into a single framework, revealing that both are governed by a momentum-dependent Pancharatnam–Berry phase and exploring the role of intrinsic and extrinsic orbital angular moment in spin separation [17].

Another notable example is to manipulate the lateral shift (shift parallel to the incident plane) known as the Goos–Hänchen (GH) effect of a light beam reflected or refracted from the interface of different media and structures [18]. In another study, it has been examined that a cross-anisotropic metasurface (CM) coating influences both spatial and angular GH shifts under total internal reflection, offering a potential method for achieving larger GH shifts and expanding CM applications [19]. Moreover, researchers have examined GH and Imbert–Fedorov shifts of rotational 2D finite energy Airy beams, exploring the impact of second-order reflection coefficient terms on their spatial shifts and revealing that both shifts are influenced by the beams' axial symmetry and can be controlled by adjusting the rotation angle of the initial field [20]. Furthermore, in another study researchers theoretically examines the spatial and angular GH shifts for an Airy beam on a weakly absorbing medium coated with monolayer graphene, highlighting significant magnification of the GH shift and its dependence on various parameters [21].

In another study GH and Imbert–Fedorov shifts for high-order off-axis Airy vortex beams has been calculated numerically, finding that both shifts increase with the vortex's topological charge and are influenced by the vortex's position relative to the origin [22]. In another study expressions for the GH and Imbert–Fedorov shifts of the Airy beam in Dirac metamaterial are analyzed, demonstrating that large shifts occur near the Dirac and Brewster angles, with potential applications for light-tuned optical switches [23]. Additionally investigations of the GH shift in the epsilon-near-zero region, revealing how graphene conductivity and Fermi energy control the shift's sign, and using this for a barcode encryption scheme based on GH shift variations [24]. However, tuning PSHE through vacuum induced transparency (VIT) in atomic cavity has not been explored in detail, which is the subject of present work.

An intriguing phenomenon in light-atom interaction systems is the quantum coherence effect, which plays a pivotal role in modulating the optical properties of a medium. A well-known example is electromagnetically induced transparency (EIT) [25,26], observed in a Λ -type three-level atomic configuration. The arrangement involves an interaction between the ground and excited states with a weak probing beam, while a strong coherent control laser couples the excited state to a metastable state. Under specific conditions, destructive interference between two absorption pathways renders the atomic medium transparent to the weak probe laser within a narrow frequency range. The few-photon regime in a high-quality cavity has been included in the most recent development of EIT [26]. Here, a single quantized cavity mode with a small number of photons substitutes in with the controlling laser. An extreme manifestation of this phenomenon, known as VIT [27,28], occurs when the controlling laser substituted through a vacuum-induced field in the cavity, enabled by strong atom–cavity coupling.

Furthermore, one may see coherence populations oscillating (CPO), a quantum coherence effect similar to the EIT phenomena, in two-level atomic systems [29,30]. Two coherent driving lasers as well as a weak probing laser are involved in the two-level system where CPO takes place. At the beat frequencies of the two lasers, these interactions generate oscillations that influence the population of the ground energy

state. The probing response of the atomic medium undergoes a significant shift, leading to a modest decrease in the absorption spectrum, when the driving field is sufficiently strong and the damping rate of the atomic coherence is significantly higher than the decay rate of the excited state population [31]. CPO has a similar effect as EIT, however, the absorption elimination does not approach zero. The VIT has been identified in a two-level system, expanding the CPO to the few-photon domain [32]. The absorption dip in such a VIT system can approach zero, providing a significant advantage over traditional CPO techniques [32].

In this paper, we investigate the PSHE phenomena in a vacuum-induced atomic cavity, where a two-level atomic ensemble as well as the cavity field interact without external factors. Within the two-level paradigm, VIT takes place when the atom–cavity coupling is strong enough and the decay rate of the cavity is much lower than the atomic decay rate. The coherent interactions in this model enable exact modulation of light polarization along with transverse shifts, providing considerable benefits for cavity QED investigations.

The vacuum-induced PSHE offers several advantages over geometric phase manipulation and WVA, primarily in terms of dynamic control, experimental simplicity, and versatility. Unlike geometric phase manipulation, which relies on precise polarization control and fixed geometric phases, vacuum-induced PSHE allows for real-time, continuous modulation of the spin–orbit coupling through the optical index of transmission, providing greater adaptability in varying experimental conditions. Additionally, vacuum-induced PSHE does not depend on weak measurements, as in WVA, making it less sensitive to noise and requiring less precision in measurement setups. This makes vacuum-induced PSHE more robust, easier to implement, and scalable across a broader range of applications, particularly in dynamic systems where rapid adjustments are crucial, such as in quantum communication, photonic quantum computing, and spin-based sensing.

The structure of this paper is as follows: In Section 2, we present our model for the two-level atomic system and compute the atomic susceptibility of the intracavity medium for PSHE. Section 3 details the theoretical calculation of PSHE. Section 4 discusses the results of manipulating PSHE within the vacuum-induced atomic cavity. Section 5 details possible experimental realization of the proposed scheme. Finally, Section 6 summarizes our findings and conclusions.

2. Dynamics and optical response of vacuum induced atomic cavity

Fig. 1(a) illustrates an atomic two-level ensemble coupled to a high-quality optical cavity, interacting through a cavity field with a single mode without external driving, while Fig. 1(b) depicts the probing of the cavity-coupled atoms by a weak laser field.

The VIT for the probe beam arises from a vacuum-induced Raman process, where the incoming probe photon is absorbed, quickly emitted into the cavity, reabsorbed by the atomic ensemble, and collectively reemitted into the probe mode. This process leads to transparency via destructive interference in the excited state $|2\rangle$, associated with the transition $|1\rangle \rightarrow |2\rangle$. When the collective coupling between atoms and cavity is strong enough as well as the decay rate of the cavity is significantly lower than the rate of atomic dissipation, VIT is prominently apparent. The enhancement of the PSHE using VIT is based on the ability of VIT to modify the medium's optical properties, particularly absorption and dispersion, through quantum interference. PSHE refers to the spatial separation of photons with different polarizations due to the spin–orbit interaction of light, which becomes significant in systems where photon polarization (spin) interacts with transverse spatial degrees of freedom. By leveraging VIT to alter the optical response of the medium, the transverse spatial separation of different polarization states can be controlled more effectively, enabling enhanced polarization-sensitive beam manipulation.

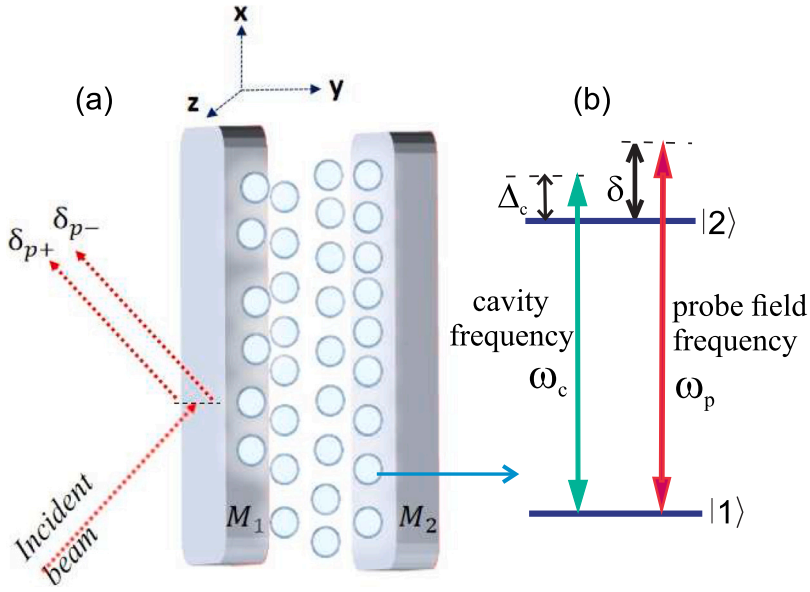


Fig. 1. (a) Schematic of a three-layer cavity system with two mirrors M_1 with M_2 , and coherent two-level atoms arranged between dielectric layers. When TM-polarized incoming light is reflected on the mirror surface M_1 , it splits spin-dependently. (b) Schematic of a two-level atomic system. The system consists of an atomic two-level ensemble coupled to a high-quality optical cavity and examined by a weak probing laser.

The system is governed by the following model Hamiltonian:

$$\begin{aligned} \mathcal{H} = & \frac{\hbar\omega_a}{2} \sum_k \tau_z^{(k)} + \hbar\omega_c \hat{n}_c - \hbar g \sum_k \left(\tau_+^{(k)} c + \tau_-^{(k)} c^\dagger \right) \\ & - \hbar\Omega \sum_k \left(\tau_+^{(k)} e^{-i\omega_p t} + \tau_-^{(k)} e^{i\omega_p t} \right). \end{aligned} \quad (1)$$

Here $\tau_z^{(k)} = |2\rangle_{kk}\langle 2| - |1\rangle_{kk}\langle 1|$, $\tau_+^{(k)} = |2\rangle_{kk}\langle 1|$, and $\tau_-^{(k)} = |1\rangle_{kk}\langle 2|$ are the Pauli matrices for the k th atom, with $|1\rangle_k$ and $|2\rangle_k$ representing ground and excited states. $\tau_z^{(k)}$, $\tau_+^{(k)}$, and $\tau_-^{(k)}$ are used to describe the internal state transitions of each atom in the ensemble. These matrices represent the quantum mechanical operators for the ground and excited states of the atom. The term $\hat{n}_c = c^\dagger \hat{c}$ refers to the number operator for the cavity field, with \hat{c}^\dagger along with \hat{c} represent the bosonic creation as well as annihilation operators of the cavity field with single-mode. The parameters ω_a , ω_c and ω_p correspond to the frequency of the atomic transition, the frequency of the cavity field, and the frequency of probe field. The expression $\Omega = \mu_{12}E/(2\hbar)$ denotes the strength of the coupling (Rabi frequency) among the atom as well as the probe laser, whereas g , which is associated with the vacuum Rabi frequency, gives the strength of coupling with regard to the atom along with the cavity. Here, E is the probe field intensity, expressed as $E = \mathcal{E}e^{-i\omega_p t}/2 + \text{c.c.}$, where the atomic transition dipole moment is μ_{12} while the field amplitude is \mathcal{E} . To ensure that the coupling coefficients g along with Ω are the same for every atom, we use the rotating-wave approach as well as assume that the optical wavelength is much larger than the size of the atomic ensemble.

In order to simplify the Hamiltonian (1), we define the atomic ensemble's collective operators as:

$$\mathcal{A} = \frac{1}{\sqrt{\mathcal{N}}} \sum_k \tau_-^{(k)}, \quad \mathcal{A}^\dagger = \frac{1}{\sqrt{\mathcal{N}}} \sum_k \tau_+^{(k)}, \quad (2)$$

where \mathcal{N} is the number of atoms in the ensemble. \mathcal{A} and \mathcal{A}^\dagger describe the collective behavior of the atomic ensemble, treating all atoms as a single effective "mode" that behaves according to bosonic statistics. This simplification is crucial for reducing the complexity of the system when dealing with many atoms.

In the regime of large \mathcal{N} and low excitation, the collective operators approximately satisfy bosonic commutation relation $[\mathcal{A}, \mathcal{A}^\dagger] \approx 1$, and we further approximate $\sum_k \sigma_z^{(k)} \approx 2\mathcal{A}^\dagger \mathcal{A} - \mathcal{N}$. Using these collective bosonic operators, Hamiltonian (1) can be expressed as

$$\mathcal{H} = \hbar\omega_a \mathcal{A}^\dagger \mathcal{A} + \hbar\omega_c \hat{n}_c - \hbar g \sqrt{\mathcal{N}} (\mathcal{A}^\dagger \hat{c} + \mathcal{A} \hat{c}^\dagger)$$

$$- \hbar\Delta_c \sqrt{\mathcal{N}} (\mathcal{A}^\dagger e^{-i\omega_p t} + \mathcal{A} e^{i\omega_p t}). \quad (3)$$

The factor $\sqrt{\mathcal{N}}$ in the Hamiltonian indicates that the interaction strength between the atoms and the cavity field is enhanced due to the collective behavior of the atomic ensemble, making the system more responsive to external fields. This modified Hamiltonian given in Eq. (3), describes a system between two interacting bosonic modes, one representing the atomic ensemble and the other representing the cavity field, where the dynamics of the system can be explored using a single probe laser. This simplified description of the system offers clearer insight into the interaction between the cavity and the atomic ensemble, while maintaining the necessary detail for accurate predictions and further analysis.

The quantum Langevin equations, which include interactions with external reservoirs (such as ambient noise) and explain how the atomic along with cavity modes change over time, control the system's dynamics:

$$\begin{aligned} \dot{\mathcal{A}} = & -i\omega_a \mathcal{A} + ig\sqrt{\mathcal{N}} \hat{c} + i\Omega\sqrt{\mathcal{N}} e^{-i\omega_p t} - \gamma \mathcal{A} + \sqrt{2\gamma} \mathcal{A}_{in}, \\ \dot{\hat{c}} = & -i\omega_c \mathcal{A} + ig\sqrt{\mathcal{N}} \mathcal{A} - \kappa \hat{c} + \sqrt{2\kappa} c_{in}, \end{aligned} \quad (4)$$

where \mathcal{A} and \hat{c} represent the collective atomic and cavity modes, respectively. The atomic damping rate along with the cavity decay rate are indicated by the parameters γ as well as κ . The terms \mathcal{A}_{in} and c_{in} represent noise operators (with zero mean) that model the coupling to the environment. The assumption here is that atomic collisional dephasing is negligible, meaning that γ and κ are the dominant loss processes.

Next the system's susceptibility, which quantifies the optical response of the atomic ensemble, obtained by means of quantum Langevin mathematical formulas (4). By calculating the mean values of the operators in the equations:

$$\begin{aligned} \langle \dot{\mathcal{A}} \rangle = & -i\omega_a \langle \mathcal{A} \rangle + ig\sqrt{\mathcal{N}} \langle \hat{c} \rangle + i\Omega\sqrt{\mathcal{N}} e^{-i\omega_p t} - \gamma \langle \mathcal{A} \rangle, \\ \langle \dot{\hat{c}} \rangle = & -i\omega_c \langle \mathcal{A} \rangle + ig\sqrt{\mathcal{N}} \langle \mathcal{A} \rangle - \kappa \langle \hat{c} \rangle, \end{aligned} \quad (5)$$

and considering $\langle \dot{\mathcal{A}} \rangle$ combined with $\langle \dot{\hat{c}} \rangle \propto e^{-i\omega_p t}$, we can easily determine the steady-state average value of the cumulative function \mathcal{A} as

$$\langle \mathcal{A} \rangle = \frac{i\Omega\sqrt{\mathcal{N}}}{\gamma - i\delta + \frac{\mathcal{N}g^2}{\kappa - i(\delta - A_c)}}, \quad (6)$$

where $\delta = \omega_p - \omega_a$ is the atomic transition and the probing field detuning, whereas $\Delta_c = \omega_c - \omega_a$ symbolizes the atomic transition and cavity field detuning. The term $P = (1/V) \sum_k \mu_{12}(\langle \sigma_-^{(k)} \rangle + \langle \sigma_+^{(k)} \rangle)$ correlates to the atomic ensemble's polarization, where V is the ensemble's volume. The positive frequency component of the polarization is given by $P^+ = \sum_k \mu_{12} \langle \sigma_-^{(k)} \rangle / V$, which can be expressed in terms of the collective operators \mathcal{A} as $P^+ = \mu_{12} \sqrt{\mathcal{N}} \langle \mathcal{A} \rangle / V$.

To connect the polarization to the probe field intensity, we use the relationship $P^+ = \chi \epsilon_0 E^+$, where $E^+ = \mathcal{E} e^{-i\omega_p t} / 2$ is the positive frequency component of the probe field intensity. Solving for the susceptibility χ , we find

$$\chi = D \frac{i}{\gamma - i\delta + \frac{\mathcal{N} g^2}{\kappa - i(\delta - \Delta_c)}}, \quad (7)$$

where $D = (\mu_{12}^2 / \hbar \epsilon_0) (\mathcal{N} / V)$ is a constant that depends on the atomic dipole moment and the density of the atoms. The term g^2 , which is the denominator of Eq. (7), represents coupling strength between the atom along with cavity, and the factor \mathcal{N} shows that collective enhancement of coupling is possible for a large ensemble. Hence, the collective atom-cavity coupling strength is denoted by $\mathcal{N} g^2$. When $g = 0$, Eq. (7) simplifies for the outcome of bare atoms, demonstrating that the cavity's presence significantly modifies the optical behavior of the atoms, even if the cavity is initially in the vacuum state. The phenomenon known as the VIT is essential for many quantum optical applications.

3. Modeling the photonic spin Hall effect

We now examine the behavior of a probe light beam, illustrated in Fig. 1(a), which is a combination of TE and TM polarizations. This beam, originating in a vacuum, strikes the cavity mirror M_1 at an angle of incidence θ_i , as depicted in Fig. 1(b). The probe beam is modeled as a monochromatic Gaussian beam, which can either transmit through the atomic system or reflect off its surface. Upon reflection, the right- and left-circular polarization components diverge spatially along the axis perpendicular to the plane of incidence (the y-axis), as illustrated in Fig. 1(b). The PSHE arises due to the spin-orbit interaction of light, leading to a polarization-dependent separation of photons with opposite helicities. For the three-layer structure considered here, the reflection coefficients for TM-polarized light, R_M , and TE-polarized light, R_s , can be derived using the Transfer Matrix Method, giving

$$R_{p,s} = \frac{R_{12,p,s} + R_{23,p,s} e^{2ik_2q}}{1 + R_{12,p,s} R_{23,p,s} e^{2ik_2q}}. \quad (8)$$

Let q in above equation represents the thickness of the intracavity medium, while $R_{12,p,s}$ and $R_{23,p,s}$ denote the reflection coefficients for the interfaces between mirror one and the intracavity two-level atoms, and between the atoms and mirror two, respectively. For a two-layer system, the reflection coefficient at the top mirror-medium-lower mirror interface for TM polarization is given by:

$$R_{ij,p} = \frac{\epsilon_j k_{iz} - \epsilon_i k_{jz}}{\epsilon_j k_{iz} + \epsilon_i k_{jz}}, \quad (9)$$

whereas for TE polarization, the reflection coefficient is expressed as:

$$R_{ij,s} = \frac{k_{iz} - k_{jz}}{k_{iz} + k_{jz}}. \quad (10)$$

In this context, the normal wave vector for each layer is given by $k_{iz} = \sqrt{k_0^2 \epsilon_i - k_x^2}$, where $k_x = \sqrt{\epsilon_1} k_0 \sin(\theta_i)$ represents the wave vector component along the x-axis. Here, $k_0 = 2\pi/\lambda$ is the free-space wave number, with λ being the wavelength of light. From the expression in Eq. (8), we observe that the reflection coefficients are influenced by the permittivity of the two-level atomic medium, ϵ_2 . This permittivity can be effectively controlled by varying the susceptibility χ , which in turn enables the manipulation of the PSHE of light.

When a TM-polarized Gaussian beam reflects off the interface between two surfaces, the field amplitudes for the two circular polarization components of the reflected light are distributed in the following way within the reflection system:

$$\begin{aligned} \mathcal{E}_r^\pm(x_r, y_r, z_r) &= \frac{\omega_0}{\omega} \exp\left[-\frac{x_r^2 + y_r^2}{\omega}\right] \times \\ & \left[R_p - \frac{2ix_r}{k\omega} \frac{\partial R_p}{\partial \theta} \mp \frac{2y_r \cot[\theta]}{k\omega} \right] \times \\ & (R_s + R_p), \end{aligned} \quad (11)$$

where $\omega = \omega_0 [1 + (2z_r/k_1 \omega_0^2)^2]^{1/2}$, $z_r = k_1 \omega_0^2 / 2$ shows the Rayleigh length, ω_0 denotes the radius of the waist of the incident beam, (x_r, y_r, z_r) is the coordinate system for reflected light and \pm represents the different spin states. The transverse shift of the reflected light can then be written as:

$$\delta_{p\pm} = \frac{\int y |\mathcal{E}_r^\pm(x_r, y_r, z_r)|^2 dx_r dy_r}{\int |\mathcal{E}_r^\pm(x_r, y_r, z_r)|^2 dx_r dy_r}. \quad (12)$$

Using Eqs. (11) and (12), the transverse spin displacement components, δ_{p+} and δ_{p-} , can be formulated in terms of the refractive coefficients of the three-layer cavity system [14,33]

$$\delta_{p\pm} = \mp \frac{k_1 \omega_0^2 \text{Re}\left[1 + \frac{R_s}{R_p}\right] \cot \theta_i}{k_1^2 \omega_0^2 + \left|\frac{\partial \ln R_p}{\partial \theta_i}\right|^2 + \left|1 + \frac{R_s}{R_p}\right| \cot \theta_i}. \quad (13)$$

In the above equation, $\delta_{p\pm}$ represents the transverse displacement between the left and right circularly polarized components of the incident light, where $k_1 = \sqrt{\epsilon_1} k$. For the purposes of this discussion, we focus on the transverse shift δ_{p+} of the left circularly polarized component. Since the magnitudes of the two spin components are identical but their directions are opposite, the shift of the right circularly polarized component can be adjusted in parallel. Furthermore, the permittivities of the cavity walls, ϵ_1 and ϵ_3 , are considered fixed, while the permittivity of the intracavity medium, ϵ_2 , is related to the susceptibility of the two-level atomic system through the following equation:

$$\epsilon_2 = 1 + \chi. \quad (14)$$

where χ is featured in Eq. (7).

4. Results

In Fig. 2(a), the susceptibility is represented by both its real and imaginary components. The real part (shown by the orange dashed line) corresponds to the dispersion, while the imaginary part (depicted by the red solid line) illustrates the absorption characteristics. Regarding bare atoms, where no cavity is present (i.e., $g = 0$), the imaginary component, $\text{Im}[\chi]$, shows an absorption-indicating Lorentzian curve with a peak at the atomic resonance frequency. On the other hand, the real component, $\text{Re}[\chi]$, exhibits anomalous dispersion behavior near the resonance frequency.

Fig. 2(b) illustrates the magnitudes of the reflection coefficients for both TE-polarized (R_s) and TM-polarized (R_p) light. The data reveals a clear distinction in the behavior of the two polarizations. For TM-polarized light (represented by the red solid line), the reflection coefficient initially decreases as the angle of incidence increases, reaching zero at the Brewster angle ($\theta_B \approx 33.8797^\circ$). After this critical angle, the coefficient begins to rise again as the angle continues to increase. Conversely, for TE-polarized light, shown by the orange dashed line, the reflection coefficient consistently increases with the angle of incidence. These opposing trends for TE and TM polarizations underscore the dependence of light reflection on the angle of incidence and the polarization state.

The transverse shift $\delta_{p\pm}$, as expressed in Eq. (13), depends on the ratio of the reflection coefficients for TE- and TM-polarized light, denoted as R_s and R_p , respectively, at a given incident angle. A significant

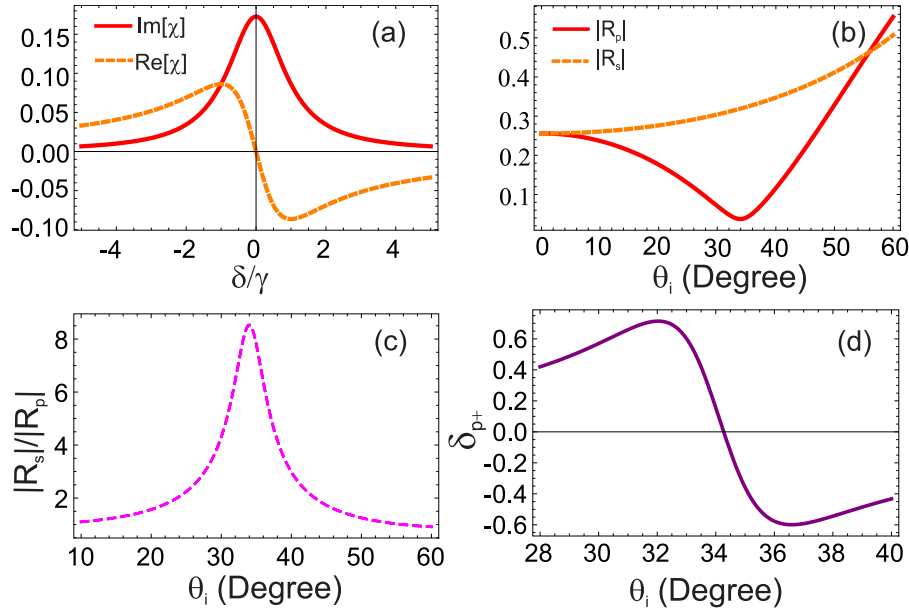


Fig. 2. (a) The absorption (solid curve) along with dispersion (dashed curve) features of an atom's cavity susceptibility as a consequence of probing field detuning δ/γ for $\mathcal{N}g^2 = 0$. The other parameters are $\kappa = 0.01\gamma$, $\gamma = 1$ MHz, $\Delta_c = 0$, $\mathcal{N}/V = 10^{12}$ cm $^{-3}$ and $\mu_{12} = 1.269 \times 10^{-29}$ cm. (b) The Fresnel coefficients $|R_s|$ and $|R_p|$ vary with incidence angle θ_i while (c) ratio $|R_s|/|R_p|$ depends on incidence angle θ_i . (d) Plot the PSHE δ_{p+} as a function of incidence angle θ_i , which changes sign from positive to negative near the angle at which the ratio $|R_s|/|R_p|$ is highest. In Fig. 2(b,c,d), we consider $\delta = 0$. Other parameters include $\epsilon_1 = \epsilon_2 = 2.22$, $\lambda = 852$ nm, $q = 0.1$ μ m, and beam waist $\omega_0 = 60\lambda$.

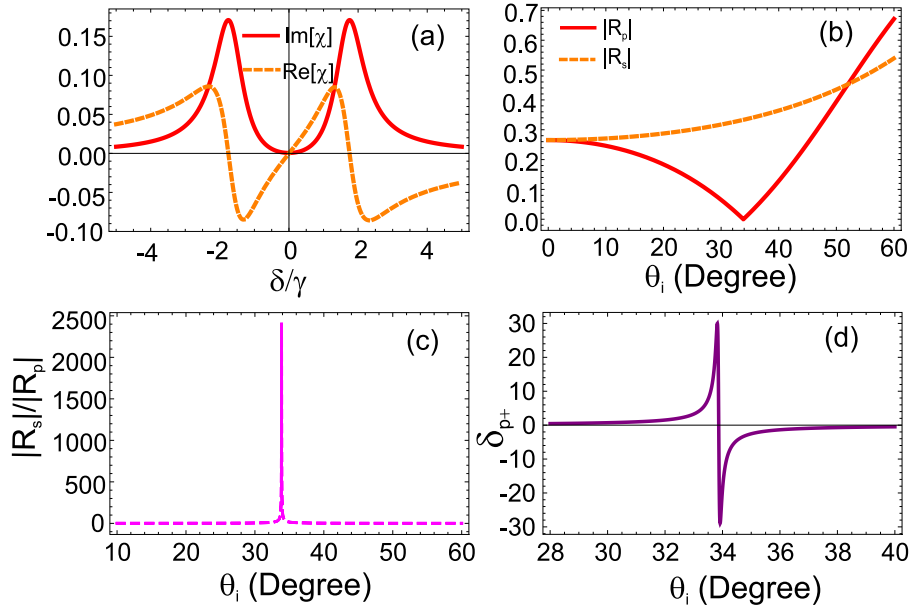


Fig. 3. (a) The absorption (solid curve) along with dispersion (dashed curve) features of an atom's cavity susceptibility as a consequence of probe field detuning δ/γ for $\mathcal{N}g^2 = 30\kappa\gamma$, $\kappa = 0.01\gamma$, along with $\Delta_c = 0$, $\gamma = 1$ MHz, $\mathcal{N}/V = 10^{12}$ cm $^{-3}$, as well as $\mu_{12} = 1.269 \times 10^{-29}$ cm. (b) The Fresnel coefficients $|R_s|$ along with $|R_p|$ vary with incidence angle θ_i and (c) the ratio $|R_s|/|R_p|$ as a function of incidence angle θ_i . (d) Plot of PSHE δ_{p+} versus incident angle θ_i changes sign from positive to negative about the angle where the ratio $|R_s|/|R_p|$ is highest. In Fig. 3(b,c,d), we consider $\delta = 0$. Other parameters include $\epsilon_1 = \epsilon_2 = 2.22$, $\lambda = 852$ nm, $q = 0.1$ μ m, along with beam waist $\omega_0 = 60\lambda$.

transverse shift is observed when this ratio exceeds unity. To investigate this dependence in more detail, Fig. 2(c) shows the ratio $|R_s|/|R_p|$ as a function of the incident angle θ_i , with $\delta = 0$, corresponding to the frequency detuning where absorption is maximized, as illustrated in Fig. 2(a). The maximum value of the ratio $|R_s|/|R_p|$ occurs at $\delta = 0$, as this frequency corresponds to the peak of the absorption profile. The ratio increases sharply near the Brewster angle, $\theta_B \approx 33.8797^\circ$. As shown in Fig. 2(b), the red curve for $\delta = 0$ reveals that $|R_p|$ tends toward zero at the Brewster angle, causing a rapid rise in the ratio. In contrast, the orange dashed curve for $|R_s|$ remains nonzero, leading

to an enhanced and positive ratio $|R_s|/|R_p|$ at the Brewster angle. To better understand the effects around this critical angle, we narrow our focus to a small range of incident angles, θ_i .

Next, we concentrate on the transverse shift resulting from the PSHE. To streamline our analysis, we specifically examine the shift associated with the right circularly polarized photon spin-dependent component, denoted as δ_{p+} . This selection is based on the inherent symmetry between the two circular polarization states, where the magnitudes of the transverse shifts are identical but their directions are opposite. Consequently, by focusing on the right circular polarization

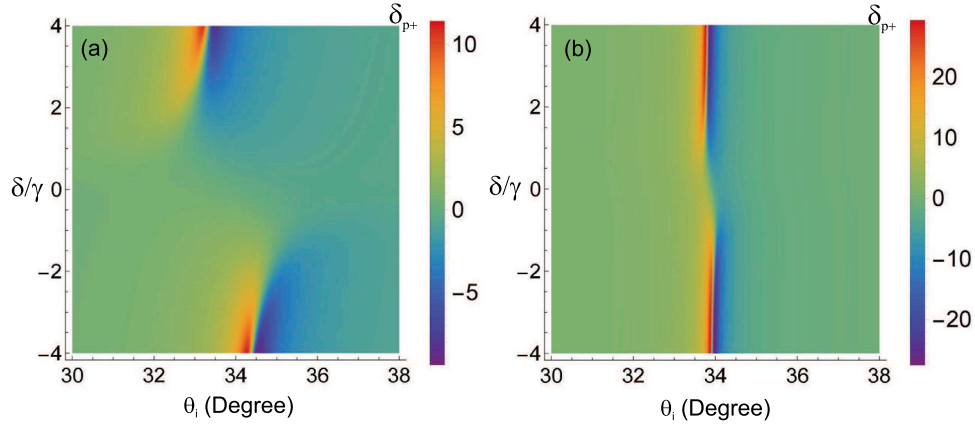


Fig. 4. (a) PSHE δ_{p+} density plot as a function of detuning δ/γ whereas incidence angle θ_i , when $\mathcal{N}/V = 10^{12} \text{ cm}^{-3}$, along with (b) PSHE δ_{p+} density diagram illustrating a decrease in number density by one order of magnitude, which is $\mathcal{N}/V = 10^{11} \text{ cm}^{-3}$. The collective cavity coupling strength $\mathcal{N}g^2 = 0$ is taken into consideration here. Beam waist $\omega_0 = 60\lambda$, $\epsilon_1 = \epsilon_2 = 2.22$, $\lambda = 852 \text{ nm}$, $q = 0.1 \mu\text{m}$, alongside $\kappa = 0.01\gamma$ are the remaining parameters.

component, we can deduce that the left circular polarization component will exhibit similar behavior, with the only difference being the reversed direction of the transverse shift.

We examine the PSHE shift, δ_{p+} , as a function of the incident angle, θ_i , shown in Fig. 2(d). For the purpose of comparison, we keep all other parameters fixed. Our analysis indicates an enhancement of the PSHE at $\delta = 0$. In particular, the transverse PSHE is positive for incident angles $\theta_i < 33.8797^\circ$, and it switches to negative for $\theta_i > 33.8797^\circ$. This reversal of sign is attributed to the π -phase difference between the phases of the Fresnel reflection coefficients, R_s and R_p , which governs the polarization-dependent reflection behavior and leads to the observed direction change in the transverse shift.

In Fig. 3(a), we observe a coherent phenomenon resembling EIT, which arises due to the influence of the cavity vacuum field. This effect manifests when the condition $\kappa \ll \gamma$ is satisfied, accompanied by a strong collectively enhanced coupling, $\mathcal{N}g^2 \geq \kappa\gamma$. For simplicity, we initially focus on the case where $\Delta_c = 0$. As illustrated in Fig. 3(a), the imaginary part of the susceptibility, $\text{Im}[\chi]$, shows a dip, while the real part, $\text{Re}[\chi]$, exhibits normal dispersion near the resonance frequency.

Fig. 3(b) presents the magnitudes of the reflection coefficients for both TE-polarized (R_s) and TM-polarized (R_p) light, with the EIT-like phenomenon induced by the cavity vacuum field. The data reveals distinct behaviors between the two types of polarization. The reflection coefficient for TM-polarized light, indicated by the red solid line, shows a decrease as the angle of incidence increases, reaching zero at the Brewster angle, $\theta_B \approx 33.8797^\circ$, before increasing again as the angle continues to rise. Conversely, the TE-polarized light's reflection coefficient, represented by the orange dashed line, increases monotonically with the incident angle. This contrasting behavior between the TE and TM reflection coefficients underscores the angle-dependent interactions between light and the surface, which are influenced by both the polarization state of the incident light and the material properties of the system.

Fig. 3(c) illustrates the ratio $|R_s|/|R_p|$ with respect to the incidence angle θ_i , where $\delta = 0$ corresponds to the frequency detuning observed at the EIT window in Fig. 3(a). The highest value of this ratio occurs at $\delta = 0$, associated with the transparency window. A sharp increase in the ratio is observed near the Brewster angle, $\theta_B \approx 33.8797^\circ$, with this enhancement being considerably stronger than the absorptive case shown in Fig. 2(c). As seen in the red curve of Fig. 3(b) for $\delta = 0$, $|R_p|$ approaches zero at the Brewster angle, which leads to a rapid increase in the ratio. In contrast, the orange dashed curve representing $|R_s|$ remains finite, resulting in a significant and positive ratio $|R_s|/|R_p|$ at this critical angle.

Next, Fig. 3(d) shows the PSHE shift, δ_{p+} , as a function of the incident angle θ_i at resonance, where $\delta = 0$. For clarity and ease

of comparison, we keep all parameters unchanged. We observe that the PSHE is enhanced at $\delta = 0$. The transverse PSHE is positive for $\theta_i < 33.8797^\circ$ and negative for $\theta_i > 33.8797^\circ$. This sign reversal can be attributed to the phase shift induced by the light–matter interaction at the surface, which changes with the incident angle. Below the Brewster angle (approximately 33.8797°), the system exhibits a positive giant transverse shift, while beyond this angle, the shift reverses direction. This transition is due to the symmetry of polarization-dependent interactions, reflecting the physics of light–matter interaction, where different polarization states contribute to the transverse shift in distinct ways.

To explore how atomic density influences the PSHE shift, we present the density plot of the PSHE in Fig. 4(a), which shows the relationship between incident angle and probe field detuning δ for an atomic density fixed at $\mathcal{N}/V = 10^{12} \text{ cm}^{-3}$. In this scenario we consider collective atom cavity coupling strength $\mathcal{N}g^2 = 0$. At resonance ($\delta = 0$), where absorption is at its peak, a relatively small PSHE shift of 0.6λ is observed. A pronounced enhancement in the PSHE, reaching values up to $\leq 10\lambda$, is observed at detuning values of $\delta = \pm 4\gamma$, where nonzero absorption contributes to the shift.

In Fig. 4(b), we examine the effect of a lower atomic density, specifically $\mathcal{N}/V = 10^{11} \text{ cm}^{-3}$ in the absence of collective atom–cavity coupling strength. At this reduced density, the PSHE shift at $\delta = \pm 4\gamma$ increases to 25λ , while the PSHE at resonance ($\delta = 0$) remains almost unchanged at approximately $\pm 0.6\lambda$. Comparing the results from Figs. 4(a) and 4(b), we observe that the PSHE remains almost constant at resonance regardless of atomic density, where absorption is maximal and no cavity–atom coupling is considered. This is because, at resonance, the probe field experiences strong absorption, which in turn weakens the spin–orbit coupling responsible for the PSHE shift. At resonance, the PSHE shift is largely independent of atomic density, as the absorption maximizes the interaction between the probe field and the atomic medium, pushing the system toward a saturation point. This means that increasing atomic density beyond a certain threshold does not notably alter the PSHE shift. However, for detuning values of $\delta = \pm 4\gamma$, the reduction in atomic density results in diminished absorption of the probe field, which, in turn, amplifies the PSHE. At these detuned frequencies, the reduced atomic density lowers the coupling strength between the field and the atomic medium, allowing the spin–orbit interaction to become more pronounced. Consequently, the PSHE shift increases significantly, reaching as high as 25λ at lower atomic densities. This increase can be attributed to the lessened field–atom interaction at detuned frequencies, allowing the spin–orbit coupling to exert a stronger influence on the transverse shift.

In Fig. 5, displays the PSHE's density plot in relation to the incidence angle θ_i and detuning of probing field δ , which illustrates the influence

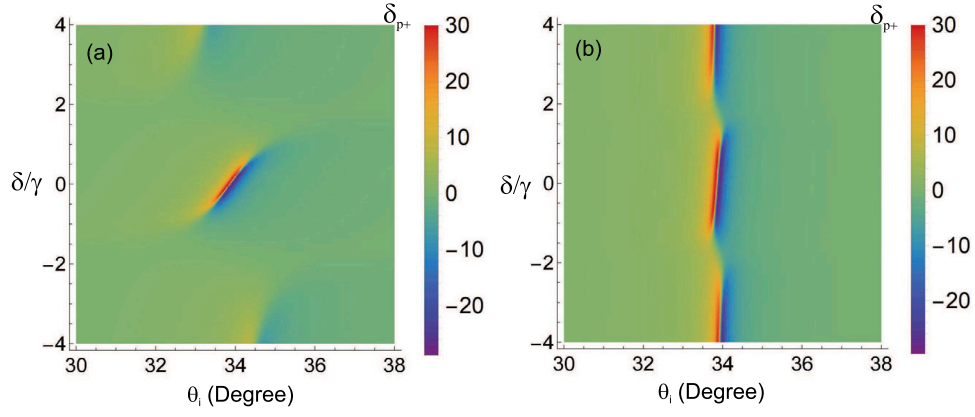


Fig. 5. (a) PSHE δ_{p+} density graph as a function of detuning δ/γ whereas incidence angle θ_i when $\mathcal{N}/V = 10^{12} \text{ cm}^{-3}$, while (b) PSHE δ_{p+} density diagram illustrating a decrease in number density by one order of magnitude, which is $\mathcal{N}/V = 10^{11} \text{ cm}^{-3}$. The collective cavity coupling strength $\mathcal{N}g^2 = 30\kappa\gamma$ that results in VIT at resonance is taken into consideration here. $\kappa = 0.01\gamma$, $\gamma = 1 \text{ MHz}$, $\epsilon_1 = \epsilon_2 = 2.22$, $\lambda = 852 \text{ nm}$, $q = 0.1 \mu\text{m}$, as well as beam waist $\omega_0 = 60\lambda$ are the additional parameters listed.

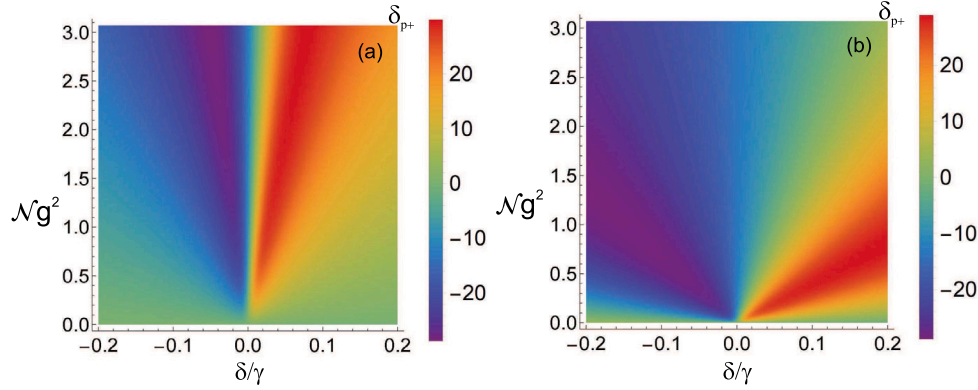


Fig. 6. The density plot of PSHE δ_{p+} with respect to the incidence angle θ_i as well as atoms cavity coupling strength $\mathcal{N}g^2$ is shown in (a) when $\mathcal{N}/V = 10^{12} \text{ cm}^{-3}$, alongside (b) when number density decreases by one order of magnitude, that is, when $\mathcal{N}/V = 10^{11} \text{ cm}^{-3}$. With $\delta/\gamma = 0$ as the other parameter, the beam waist $\omega_0 = 60\lambda$, $\kappa = 0.01\gamma$, $\gamma = 1 \text{ MHz}$, $\epsilon_1 = \epsilon_2 = 2.22$, $\lambda = 852 \text{ nm}$, as well as $q = 0.1 \mu\text{m}$.

of atomic density in the presence of collective atom–cavity coupling strength $\mathcal{N}g^2$. Fig. 5(a) shows the PSHE for a fixed atomic density of $\mathcal{N}/V = 10^{12} \text{ cm}^{-3}$. At resonance ($\delta = 0$), where EIT occurs due to VIT in the presence of atom–cavity coupling, a maximum PSHE of 30λ is observed. Smaller PSHE peaks, around $\leq 5\lambda$, are observed at detunings of $\delta = \pm 4\gamma$, resulting from some nonzero absorption at these frequencies. In contrast, Fig. 5(b) shows a similar density plot for a reduced atomic density of $\mathcal{N}/V = 10^{11} \text{ cm}^{-3}$. At this lower density, the PSHE at $\delta = \pm 4\gamma$ increases to 30λ , while the PSHE at resonance ($\delta = 0$) remains nearly constant at approximately $\pm 30\lambda$. These results suggest that atomic density plays a significant role in determining the degree of absorption, which consequently influences the strength of the spin–orbit coupling. When the atomic density is reduced, absorption decreases, making the spin–orbit coupling the dominant interaction between the probe field and the atomic medium. This leads to an enhancement of the PSHE shift, as observed at the detuned frequencies.

Fig. 6(a) illustrates the impact of atomic density on the PSHE by fixing the incident angle $\theta_i \approx 33.8797^\circ$ and varying both the atom–cavity coupling strength $\mathcal{N}g^2$ and the detuning δ/γ . The density plot of the PSHE, represented by δ_{p+} , reveals the relationship between atomic number density \mathcal{N}/V , coupling strength, and detuning conditions. At a high atomic number density of $\mathcal{N}/V = 10^{12} \text{ cm}^{-3}$, the system shows a prominent PSHE peak at resonance ($\delta = 0$), with a maximum amplitude of approximately 25λ . This is due to the strong atom–cavity coupling, which leads to VIT, thereby enhancing the PSHE at resonance. When the atomic density is reduced to $\mathcal{N}/V = 10^{11} \text{ cm}^{-3}$, the atom–cavity coupling weakens, see Fig. 6(b). As a result, the PSHE exhibits

its maximum value over a broader range of detuning, suggesting a more uniform distribution of the effect across detuning values. This shift occurs because the weaker interaction between the atoms and the cavity mode diminishes the sharp resonance effects, making the PSHE less sensitive to specific detuning and more broadly spread out.

The collective atom–cavity coupling strength, denoted as $\mathcal{N}g^2$, is a critical factor in determining the strength of the PSHE. As the atomic density increases, more atoms are coupled to the cavity field, which enhances the collective interaction and leads to a stronger spin–orbit coupling, thus resulting in a more significant PSHE shift. However, the relationship between atomic density and coupling strength is not always linear. At very high atomic densities, atomic interactions may become saturated, causing a diminishing return on coupling strength and reducing the effectiveness of the PSHE. Therefore, there exists an optimal atomic density range that balances strong collective coupling with minimal absorption, allowing for the maximum PSHE shift. This optimal density depends on factors such as detuning, cavity decay rate, and the atomic transition dipole moment, all of which influence the overall interaction strength between the probe field and the atomic medium.

In practical applications such as quantum memory and quantum sensing, understanding the optimal atomic density for maximizing PSHE is crucial. For quantum memory, an ideal atomic density ensures effective storage and retrieval of quantum states, as too high a density can lead to excessive absorption, while too low a density may not provide sufficient coupling. In quantum sensing, tuning the atomic

density can enhance the system's sensitivity to external perturbations by adjusting the PSHE shift at detuned frequencies. However, varying atomic density can introduce challenges such as thermal effects and decoherence, particularly at high densities where atomic interactions may lead to heating and performance degradation. Balancing these factors is necessary to optimize the PSHE for practical use in quantum technologies.

Here we would like to mention that PSHE through VIT in an atomic cavity represents a versatile mechanism that can be extended to various spin-dependent phenomena beyond its current application. These include optical spin-orbit torque, spin-controlled photonic circuits, and more complex systems such as multi-level atoms and coupled cavity arrays. By exploring these extensions in future, novel quantum devices that leverage the spin-orbit interaction to control light-matter interactions in highly tunable and efficient ways can be achieved. The proposed mechanism could provide new insights and tools for designing quantum memory, quantum communication systems, and spintronic devices, ultimately advancing the field of quantum photonics and spin-based technologies.

5. Experimental realization of the proposed model

We describe a potential experimental implementation of our proposed model, supported by relevant experimental references to complement the theoretical analysis. Our system can be realized by replacing the control field in a two-level atomic system with a vacuum field inside a strongly coupled cavity. In this setup, both the probe beam and the cavity mode are tuned to the $|1\rangle \rightarrow |2\rangle$ transition. A high-Q optical cavity, capable of trapping cold atoms (e.g., ^{133}Cs), can accommodate up to 10^5 atoms in a far-off-resonance optical lattice trap at 937 nm inside the cavity [27]. The two-level system is defined by the states $|1\rangle = |6S_{1/2}, F = 4, m_F = 4\rangle$ and $|2\rangle = |6P_{3/2}, F = 4, m_F = 4\rangle$. This configuration has been experimentally realized using evaporatively cooled atoms in cavities with small mode volumes [34,35]. Achieving a sufficiently strong coupling between the atomic ensemble and the cavity modes is crucial for both VIT and PSHE. Strong coupling is established when the interaction rate g exceeds both the atomic decay rate γ and the cavity decay rate κ . In practice, this requires designing cavities with extremely low decay rates, typically in the range of $\kappa \approx 10^{-3}$ to 10^{-5} for high-Q cavities. Fabricating such cavities, particularly at the micro- or nanoscale, presents significant challenges. However, recent advancements in cavity quantum electrodynamics have demonstrated that such conditions can be achieved, especially in optomechanical or superconducting cavity setups [36,37]. Additionally, decoherence effects arising from environmental interactions such as thermal fluctuations, atomic collisions, and impurities pose challenges to maintaining coherence in the system. Imperfect isolation of the atom-cavity system can further contribute to decoherence. These issues can be mitigated by employing ultra-low-temperature cooling techniques and using high-Q cavities to minimize losses. Moreover, precise control over experimental parameters, including atomic population, cavity detuning, and interaction strength, is essential for observing both VIT and PSHE. This requires advanced cooling techniques, such as laser cooling and evaporative cooling, along with meticulous fine-tuning of the atom-cavity interactions [27,34,35].

6. Conclusions

In conclusion, this paper presents a detailed analysis of how polarization-dependent reflection coefficients, atomic density, and detuning influence the PSHE. Key findings highlight the significant role of the Brewster angle in modulating the reflection coefficient ratio, which in turn enhances the transverse shift of the PSHE, particularly at resonance frequencies. The study also demonstrates how atomic density affects the PSHE, with lower densities promoting stronger spin-orbit interactions due to reduced absorption, while higher densities

suppress the effect due to increased absorption. Additionally, the introduction of cavity effects gives rise to an EIT-like phenomenon, providing a versatile mechanism for controlling spin-dependent light-matter interactions. These insights deepen our understanding of the factors governing the PSHE and offer potential pathways for tuning this effect in practical cavity QED setups.

CRediT authorship contribution statement

Muqaddar Abbas: Writing – review & editing, Writing – original draft, Visualization, Methodology, Formal analysis, Data curation, Conceptualization. **Yunlong Wang:** Writing – review & editing, Validation, Methodology, Investigation, Formal analysis. **Feiran Wang:** Visualization, Methodology, Investigation, Data curation, Conceptualization. **Hamid R. Hamed:** Writing – review & editing, Visualization, Validation, Methodology, Investigation, Formal analysis, Conceptualization. **Pei Zhang:** Writing – review & editing, Supervision, Methodology, Investigation, Funding acquisition, Conceptualization.

Declaration of competing interest

The authors declare that they have no known competing financial interests or personal relationships that could have appeared to influence the work reported in this paper.

Acknowledgments

This work was supported by the National Natural Science Foundation of China (Grant No. 12174301), the Young Investigator (Grant No. 12305027), the Natural Science Basic Research Program of Shaanxi (Program No. 2023-JC-JQ-01), and the Fundamental Research Funds for the Central Universities.

Data availability

Data will be made available on request.

References

- [1] Onoda M, Murakami S, Nagaosa N. *Phys Rev Lett* 2004;93(8):083901.
- [2] Bliokh KY, Bliokh YP. *Phys Rev Lett* 2006;96(7):073903.
- [3] Sinova J, Valenzuela SO, Wunderlich J, Back C, Jungwirth T. *Rev Modern Phys* 2015;87(4):1213–60.
- [4] Valenzuela SO, Tinkham M. *Nature* 2006;442(7099):176–9.
- [5] Cardano F, Marrucci L. *Nat Photonics* 2015;9(12):776–8.
- [6] Bliokh KY, Rodríguez-Fortuño FJ, Nori F, Zayats AV. *Nat Photonics* 2015;9(12):796–808.
- [7] Kim M, Yang Y, Lee D, Kim Y, Kim H, Rho J. *Laser & Photonics Rev* 2023;17(1):2200046.
- [8] Sheng L, Chen Y, Yuan S, Liu X, Zhang Z, Jing H, et al. *Prog Quantum Electron* 2023;100484.
- [9] Liu S, Chen S, Wen S, Luo H. *Opto- Electron Sci* 2022;1(7):220007.
- [10] Cai L, Liu M, Chen S, Liu Y, Shu W, Luo H, et al. *Phys Rev A* 2017;95(1):013809.
- [11] Chen S, Zhou X, Mi C, Luo H, Wen S. *Phys Rev A* 2015;91(6):062105.
- [12] Ménard J-M, Mattacchione AE, Betz M, van Driel HM. *Opt Lett* 2009;34(15):2312–4.
- [13] Zhou X, Ling X, Luo H, Wen S. *Appl Phys Lett* 2012;101(25).
- [14] Xiang Y, Jiang X, You Q, Guo J, Dai X. *Photonics Res* 2017;5(5):467–72.
- [15] Kort-Kamp WJd. *Phys Rev Lett* 2017;119(14):147401.
- [16] Tang T, Shen K, Li J, Liang X, Tang Y, Li C, et al. *Opt Express* 2023;31(24):40308–16.
- [17] Zhang Z, Tan Y, Ling X, Deng D. *Opt Laser Technol* 2024;176:110987.
- [18] Asiri S, Wang L-G. *Sci Rep* 2023;13(1):22780.
- [19] Zhen W, Deng D, Guo J. *Opt Laser Technol* 2021;135:106679.
- [20] Gao M, Deng D. *Opt Express* 2020;28(7):10531–41.
- [21] Zhen W, Deng D. *Opt Express* 2020;28(16):24104–14.
- [22] Gao M, Wang G, Yang X, Liu H, Deng D. *Opt Express* 2020;28(20):28916–23.
- [23] Yue Q, Zhou X, Deng D. *New J Phys* 2023;25(1):018001.
- [24] Ding Y, Deng D, Zhou X, Zhen W, Gao M, Zhang Y. *Opt Express* 2021;29(25):41164–75.
- [25] Harris SE. *Phys Today* 1997;50(7):36–42.
- [26] Fleischhauer M, Imamoglu A, Marangos JP. *Rev Modern Phys* 2005;77:633–73.

- [27] Tanji-Suzuki H, Chen W, Landig R, Simon J, Vuletić V. *Science* 2011;333(6047):1266–9.
- [28] Field J. *Phys Rev A* 1993;47(6):5064.
- [29] Schwarz S, Tan T. *Appl Phys Lett* 1967;10(1):4–7.
- [30] Boyd RW, Raymer MG, Narum P, Harter DJ. *Phys Rev A* 1981;24(1):411.
- [31] Agarwal GS, Dey TN. *Laser & Photonics Rev* 2009;3(3):287–300.
- [32] Guo Y-J, Nie W-J. *Chin Phys B* 2015;24(9):094205.
- [33] Wu L, Chu HS, Koh WS, Li EP. *Opt Express* 2010;18(14):14395–400.
- [34] Brennecke F, Donner T, Ritter S, Bourdel T, Köhl M, Esslinger T. *Nature* 2007;450(7167):268–71.
- [35] Colombe Y, Steinmetz T, Dubois G, Linke F, Hunger D, Reichel J. *Nature* 2007;450(7167):272–6.
- [36] Romagnoli P, Maeda M, Ward JM, Truong VG, Nic Chormaic S. *Appl Phys B* 2020;126(6):111.
- [37] Spencer MS, Urban JM, Frenzel M, Mueller NS, Minakova O, Wolf M, et al. *Light: Sci Appl* 2025;14(1):69.